PROTEINS: Structure, Function, and Genetics 48:15-30 (2002)

Anti-Cooperativity and Cooperativity in Hydrophobic Interactions: Three-Body Free Energy Landscapes and Comparison With Implicit-Solvent Potential Functions for Proteins

Seishi Shimizu and Hue Sun Chan*

Department of Biochemistry and Department of Medical Genetics and Microbiology, Faculty of Medicine, University of Toronto, Toronto, Ontario, Canada

ABSTRACT **Potentials of mean force (PMFs) of three-body hydrophobic association are investigated to gain insight into similar processes in protein folding. Free energy landscapes obtained from explicit simulations of three methanes in water are compared with that predicted by popular implicit-solvent effective potentials for the study of proteins. Explicit-water simulations show that for an extended range of three-methane configurations, hydrophobic association at 25°C under atmospheric pressure is mostly anti-cooperative, that is, less favorable than if the interaction free energies were pairwise additive. Effects of free energy nonadditivity on the kinetic path of association and the temperature dependence of additivity are explored by using a three-methane system and simplified chain models. The prevalence of anti-cooperativity under ambient conditions suggests that driving forces other than hydrophobicity also play critical roles in protein thermodynamic cooperativity. We evaluate the effectiveness of several implicit-solvent potentials in mimicking explicit water simulated three-body PMFs. The favorability of the contact free energy minimum is found to be drastically overestimated by solvent accessible surface area (SASA). Both the SASA and a volume-based Gaussian solvent exclusion model fail to predict the desolvation barrier. However, this barrier is qualitatively captured by the molecular surface area model and a recent "hydrophobic force field." None of the implicit-solvent models tested are accurate for the entire range of three-methane configurations and several other thermodynamic signatures considered. Proteins 2002;48:15-30.** © 2002 Wiley-Liss, Inc.

Key words: hydrophobicity; energy landscape; nonadditivity; calorimetry; many-body interactions

INTRODUCTION: ROLE OF HYDROPHOBIC INTERACTIONS IN PROTEIN FOLDING

The proposition that hydrophobic effects have a prominent role in protein folding is indisputable.[1–9] Yet more detailed understanding is needed to ascertain the importance of their contribution in underpinning typical protein properties vis-à-vis those from other energetic components such as hydrogen bonding.[10,11] An issue central to the formation of protein native cores and many other aspects of folding is whether hydrophobic associations are approximately additive, cooperative, or anti-cooperative. These descriptions refer to the following three *a priori* possibilities, which in general depend on temperature, pressure, the specific spatial configuration, and the nature of the hydrophobic groups involved.[12,13] (i) Additive: the actual interaction free energy of a collection of hydrophobic groups is well approximated by the sum of their interaction free energies taken one pair at a time. (ii) Cooperative: the actual free energy is more favorable to association (more negative or less positive) than the pairwise sum. (iii) Anti-cooperative: the actual free energy is less favorable to association (more positive or less negative) than the pairwise sum.#

To date, "big-picture" analyses of the balance of forces in proteins[1–6,10] have largely been cast in discourses that presume additivity tacitly, although the need to account for potential nonadditivity effects has been recognized,[15–19] especially with regard to entropic contributions.[15,16] The implications of nonadditivity are broad and far reaching. One particular aspect that motivated the present investigation was our group's recent studies indicating that additive

Grant sponsor: Connaught Fund; Grant sponsor: Medical Research Council of Canada; Grant number: MT-15323.

*Correspondence to: Hue Sun Chan, Department of Biochemistry and Department of Medical Genetics and Microbiology, Faculty of Medicine, University of Toronto, Toronto, Ontario M5S 1A8, Canada. E-mail: chan@arrhenius.med.toronto.edu

Received 3 July 2001; Accepted 10 January 2002

#To avoid confusion, here we do not use the term "negative cooperativity" for anti-cooperativity because the free energy of favorable multiple-body cooperative interactions are more negative than the corresponding sum of pairwise interaction free energies. The present definition of interaction anti-cooperativity is formally similar to the usage of the term "anti-cooperativity" in ligand binding (see, e.g., p. 862 of Cantor and Schimmel[14]). However, there is an important physical distinction. In ligand binding, "cooperativity," "additivity," or "anti-cooperativity" are usually defined by comparing macroscopic binding constants, which include contributions from configurational entropies of the ligands and substrates and, therefore, involve many ligand/substrate configurations. On the other hand, cooperativity, additivity, or anti-cooperativity are determined here by comparing interaction free energies for a given configuration of hydrophobic solutes by Boltzmann averaging only over solvent (water) configurations.

contact interactions, especially those with low energetic heterogeneity,[20–22] are by themselves insufficient to account for the calorimetic and other hallmarks of thermodynamic two-state cooperativity that have been experimentally observed for many small proteins.[23–26] This suggests that, even at a coarse-grained level, our understanding of protein energetics is far from adequate.[26,27]

The focus of the present work is on the physical hydrophobic potential of mean force (PMF). Therefore, our results may bear on the physical plausibility of the functional forms used for various postulated cooperative interactions in protein-folding models.[23,25,28–31] In a similar vein, the present analysis may also shed light on knowledge-based statistical potentials[32–36] that have terms involving more than two interacting entities (see, e.g., Kolinski et al.[37] and Gan et al.[38]), and the proposal that successful fold recognition fundamentally requires non-pairwise-additive energies in the scoring function.[39]

EXPLICIT-WATER SIMULATIONS OF NONADDITIVE HYDROPHOBIC EFFECTS

In earlier studies of hydrophobic effects, questions regarding additivity and spatial dependence were sometimes discussed in terms of the differences between "pair" and "bulk" hydrophobic interactions.[40] To explore these differences, many-body hydrophobic interactions have been simulated by using high-concentration mixtures of hydrophobic solutes and water molecules.[41–45] Among these efforts, of particular relevance is a simulation of the concentration dependence of methane aggregation by Tsai et al.,[44] who concluded that hydrophobic association is "cooperative."[44,45] However, it is important to note that the Tsai et al. usage of the term "cooperative" is different from the present one. Their meaning is more akin to that in ligand-binding studies (see above) or that refers to the sharpness of thermodynamic transitions between macroscopic states. Thus, what they meant by "cooperative," is at variant[12,13] with the commonly adopted meaning of cooperativity of effective intrachain interaction in protein folding.[12,28–31,46] Indeed, this is quite clear from their recent attempt[45] to use a common implicit-solvent surface area model to account for their simulated aggregation data without considering the possibility of interaction nonadditivity. The two different usages of the term "cooperative" has also been clarified by a simple lattice model of binary solution,[13] which shows that cooperative interactions (present meaning) are not necessary for solvophobic aggregation and that additive (non-cooperative) favorable interactions between solutes can lead to a sharp transition between a dispersed (solvated) state and a collapsed (aggregated) state of the binary mixture, similar to that observed in the Tsai et al. simulations. These model results further show that the aggregation transition of independent (unconnected) solutes as a function of the solvophobic solute concentration are much sharper than the average collapse transition of connected chains of solutes as a function of solute composition. This is a consequence of the severe chain connectivity constraints on configurational entropy.[13] Taken together, our recent statistical mechanical considerations[13] do not support the suggestion by Tsai et al.[44] that there is a direct physical correspondence between typical protein core sizes and the sizes of simulated aggregated clusters of hydrophobic solutes that are not covalently linked.

Three-body hydrophobic effects have been analyzed by using molecular simulations of three-methane systems at 25°C or 298 K under atomspheric pressure (1 atm), similar to the one studied here, first by Rank and Baker[47] and subsequently by Czaplewski et al.[46] However, their conclusions disagree. The inconsistency between these two studies is difficult to resolve unequivocally within the confines of their approaches because of intrinsic uncertainties in assigning zero-PMF baselines, as noted by these authors. Obviously, in the absence of accurate and consistent zero-PMF baselines, it is not possible to use comparisons of two- and three-body PMFs to ascertain deviations from additivity. Recently, we have made progress toward overcoming this problem by using the test-particle insertion technique,[48–50] which allows for an unambiguous (i.e., theoretically justifiable) and numerically more reliable determination of zero-PMF baselines. For most of the three-methane configurations that we examined under the same conditions, we found that hydrophobic associations are anti-cooperative. In addition, based on comparing experimental data and simulated two-methane PMFs, hydrophobic anti-cooperativity is also seen to be operative in the formation of large clusters of close-packed methane molecules in water at 25°C and 1 atm.[12] Here these results are confirmed by much more extensive simulations of the two-methane PMF. Details of this new calculation and related methodological and technical issues are discussed in the Appendix.

Equilibrium thermodynamic properties of a protein are dictated by the shape of its free energy landscape, which provides the "internal free energy" of every protein conformation by Boltzmann averaging the solvent degrees of freedom for each conformation.[51,52] In other words, a free energy landscape thus defined is the potential of mean force of the given protein as a function of its conformational coordinates. Inasmuch as the effects of transient, non-equilibrium motions of the solvent molecules on chain dynamics are negligible, the folding/unfolding kinetics of the protein is also determined by the same landscape. Such protein free energy landscapes are clearly very high dimensional, extremely complex, and currently beyond the reach of atomic simulation. Indeed, all-atom molecular dynamics simulations of protein folding and unfolding[53,54] are computationally intensive even for a very small number of trajectories. To make progress, we take initial steps toward understanding protein free energy landscapes by considering a minimal construct for interaction nonadditivity, namely, a model system of three methanes. A main focus here is on the effectiveness of several surface area and volume-based implicit-solvent hydrophobic interaction potentials.[55–72] Despite their many limitations,[73] such as some of these approaches' failure to account for the significant effects of curvature of nonpolar surfaces,[74–77] implicit-solvent models have played a major role in shaping our conceptualization of hydrophobic interactions in proteins.[55–72] Here we assess to what degree they are

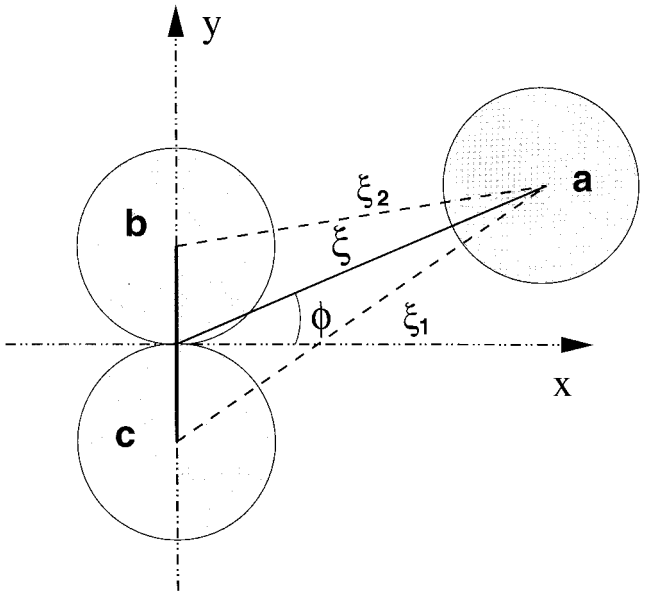

Fig. 1. The three-methane system studied in this article; *x*, *y* are Cartesian coordinates. Methanes are shown as shaded spheres; water molecules are not depicted. Geometrical variables defining the relative positions of the single methane "a" and the fixed methane dimer "b, c" (the centers of mass of "b" and "c" are 3.8 Å apart) are the same as that in Shimizu and Chan.[12]

capable of capturing nonadditive effects by comparing the predictions from several of these models against the three-methane PMF that we recently obtained by explicit-water simulations.[12]

FREE ENERGY LANDSCAPES OF THREE-METHANE ASSOCIATION

Figure 1 shows the model system studied in this article. All results in this work were obtained by constant-pressure, constant-temperature (*NPT*) Monte Carlo simulations of 396 TIP4P water molecules at 25°C (298.15 K) under atmospheric pressure in a box with periodic boundary conditions using BOSS version 4.1.[78] A united-atom representation is used for the methanes. The simulation methodology and all numerical parameters used in this article are the same as that in our recent reports.[12,49]

Let $\Delta G(x, y)$ be the free energy of bringing methane "a" from a position infinitely far away from the origin to the position (x, y) in the vicinity of a fixed methane dimer "b, c." This free energy may also be expressed in terms of the polar variables ξ and ϕ as in Figure 1. The PMF function $\Delta G(x, y) = \Delta G(\xi, \phi)$ is the free energy landscape of interest. To ascertain the degree to which this three-methane PMF deviates from additivity, $\Delta G(x, y)$ is compared against the *hypothetical* PMF computed by assuming pairwise additivity, viz.,

$$\Delta G_{\text{add}}(x,y) = \Delta G_{\text{add}}(\xi,\phi) = \Delta G_2(\xi_1) + \Delta G_2(\xi_2), \qquad (1)$$

where $\Delta G_2(\xi_1)$ and $\Delta G_2(\xi_2)$ are, respectively, the two-methane PMF for a pair of methanes at distances ξ_1 and ξ_2 apart. Here we use the two-methane PMF in the Appendix, which is of higher accuracy than the ones used in our previous studies.[12,49] Based on the quantity ΔG_{add}, a

$$\text{cooperative term} = \Delta G(x,y) - \Delta G_{\text{add}}(x,y) \qquad (2)$$

is defined as before.[12,46] For a given configuration (x, y), three-methane hydrophobic association is cooperative, additive, or anti-cooperative if this cooperative term is, respectively, less than, equal to, or greater than zero.

In calculating the PMFs for Figure 1, only angles within the range $0 \le \phi \le \pi/2$ (ϕ given in radian) need to be considered. They are sufficient to cover positions at all ϕ's because by symmetry a position at ϕ is equivalent to the positions at $-\phi$, $\phi - \pi$, and $\pi - \phi$. The present analysis is based on the three-body PMF values previouly reported[12] for $\phi = n\pi/12$, $n = 0, 1, \ldots, 5$ as well as the new $\phi = \pi/2$ data we have since obtained. The PMF calculation for $\phi = \pi/2$ requires more computational effort because it entails performing test-particle insertions along a line instead of on a two-dimensional surface as for $\phi \ne \pi/2$. Thus, a significantly longer simulation time is needed for convergence. The present $\phi = \pi/2$ results were computed by using 9.0×10^7 passes of Monte Carlo simulation, where one pass equals 396 Monte Carlo steps in our simulation.

The contour plots in Figure 2 compare the directly simulated (actual) three-methane free energy landscape with its additivity-assumed (hypothetical) counterpart. They provide a panoramic view of the two landscapes. Different landscape topographies imply different kinetics. To illustrate the kinetic ramifications of hydrophobic nonadditivity, Figure 2 shows two optimal paths that lead a methane ("a" in Fig. 1) from a common starting point (**a** in Fig. 2) to its global contact minimum position with the fixed methane dimer (**a**′ in Fig. 2). These paths are the shortest paths that minimize the total positive change in free energy along the paths on their respective landscapes. They are obtained by applying Dijkstra's algorithm to a discretized version of the landscape constituted of free energies defined on a two-dimensional grid.[†] The general procedure for constructing these minimal-climb paths is identical to that applied to the determination of optimal conformational paths in a lattice model of protein-folding kinetics.[79,80] The free energy profiles along these paths are shown in Figure 3.

At least two factors contributed to different routes being taken by the optimal paths on the actual landscape versus that on the additivity-assumed hypothetical landscape. First, for the actual landscape [Fig. 2(A)], there are considerable variations in desolvation barrier heights. As a result, when a methane is approaching the fixed methane dimer in the $-y$ direction, it may take an energetically less costly route by crossing the barrier region via a "mountain pass" at $\phi \approx 5\pi/12$. On the other hand, for the

[†]The two-dimensional grid we used for path optimization is constructed as follows. Beginning with a set of points 0.1 Å apart along the $+y$ axis, nodes on the grid are placed on concentric circles that intersect the $+y$ axis at these points, with successive radii differing by 0.1 Å. These circles are centered at one of the two fixed methanes. The arc-length spacing between successive nodes on any given concentric circle is also 0.1 Å. The grid is made up of connections from each node to exactly four nodes that are nearest to it. For present purposes, it is sufficient to confine considerations to the first quadrant of Figure 1 because of symmetry. PMF values at the grid points are obtained by interpolation from those directly simulated at $\phi = n\pi/12$ for $n = 0, 1, \ldots, 6$.

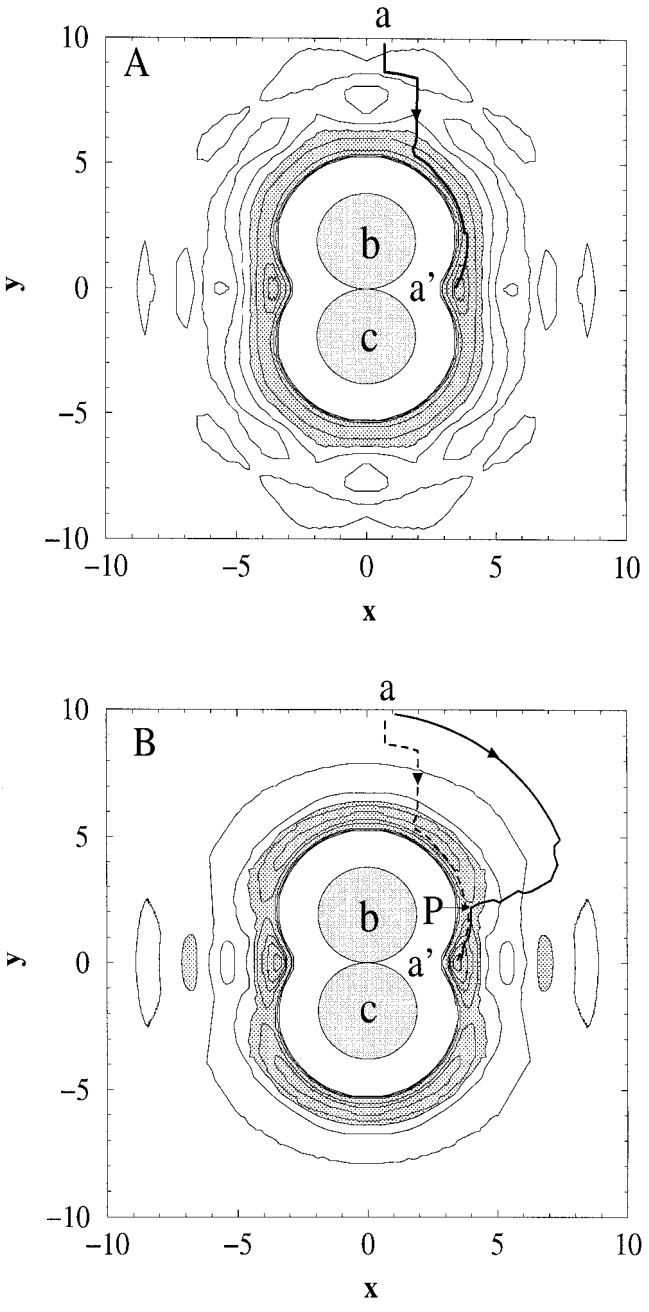

Fig. 2. Contour representations of three-methane free energy landscapes at 25°C and 1 atm: **A**: $\Delta G(x, y)$ (actual). **B**: $\Delta G_{add}(x, y)$ (hypothetical, assuming additivity). The x–y Cartesian system is the same as that in Figure 1, measured in units of Å. Contours are given at 0.25 kcal/mol intervals (at . . . , +0.25, 0.0, −0.25, . . .), for the free energy of the single methane "a" in Fig. 1 in the vicinity of the fixed methane dimer "b, c," relative to its free energy at a position infinitely far away from the dimer (c.f. Fig. 3 below and Fig. 3 of Shimizu and Chan[12]). Areas with free energy ≤ -0.25 kcal/mol are shaded. Optimized kinetic paths from a common starting point **a** on the two landscapes to the global minimum **a**′ are determined as described in the text. The sum of total free energy climbs (positive changes in free energy) along the entire length of the optimal paths (thick solid directed curves) in (A) and (B) are, respectively, 0.26 and 0.18 kcal/mol. The corresponding sum for superimposing the optimal path for A onto the hypothetical landscape (B, thick dotted directed curve) is 0.92 kcal/mol.

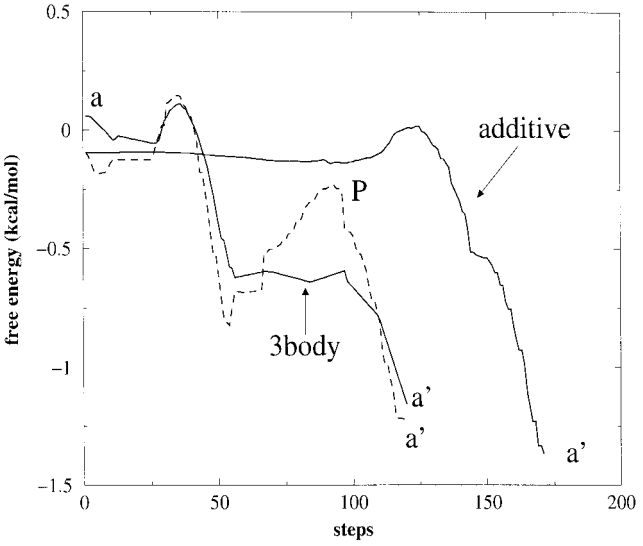

Fig. 3. Variations in free energy along the paths shown in Figure 2, as functions of the number of discretized steps along these paths on the two-dimensional grid defined in the text. The labels **a**, **a**′ for the beginning and end points of the paths and **P** for the local free energy maximum correspond to that in Figure 2. Free energy profiles labeled as "3body" and "additive" (solid curves) correspond to the optimized path on the actual and hypothetical landscapes ΔG (x ,y) and ΔG_{add} (x, y) in Figure 2(A) and (B), respectively. The dotted free energy profile corresponds to the dotted path, which is non-optimal on the hypothetical landscape $\Delta G_{add}(x,y)$ in Figure 2(B).

additivity-assumed hypothetical landscape [Fig. 2(B)], the desolvation barrier facing the approaching methane does not exhibit much angular dependence for $\phi > \pi/6$ (no "mountain pass"). This is because the hypothetical barrier in this region is contributed almost entirely by the two-body desolvation barrier between the approaching methane and the methane "b" nearest to it. This is a reason why the optimal path on the hypothetical landscape takes a more circuitous route.

Second, on the actual landscape, once contact is established, there is a general trend of increasing favorability between the single methane and the methane dimer "b, c" as the single methane approaches the global minimum. In other words, the depth of the contact "trench" increases more or less monotonically as $\phi \approx \pi/2$ decreases to $\phi = 0$. This accounts for the optimal path in Figure 2 (A), whereby the approaching methane simply slides on the surface of methane "b" into the $\phi = 0$ global minimum position after it collided with methane "b" at $\phi \approx 5\pi/12$. On the other hand, there is a significant local free energy peak at position **P** on the hypothetical additivity-assumed landscape in Figure 2(B). This renders the optimal "sliding" path for the actual landscape unfavorable on the hypothetical landscape (Fig. 3). Instead, a "flanking maneuver" is needed to circumvent this hypothetical local maximum if the single methane were to approach the global minimum via an optimal path. This is the predominant reason for the differences between the optimized paths on the actual and the hypothetical landscapes.

As we have discussed,[12] the phenomenon of a local peak **P** at $\phi \approx \pi/6$ on the hypothetical landscape [Fig. 2(B)] is a robust feature because this position coincides with the

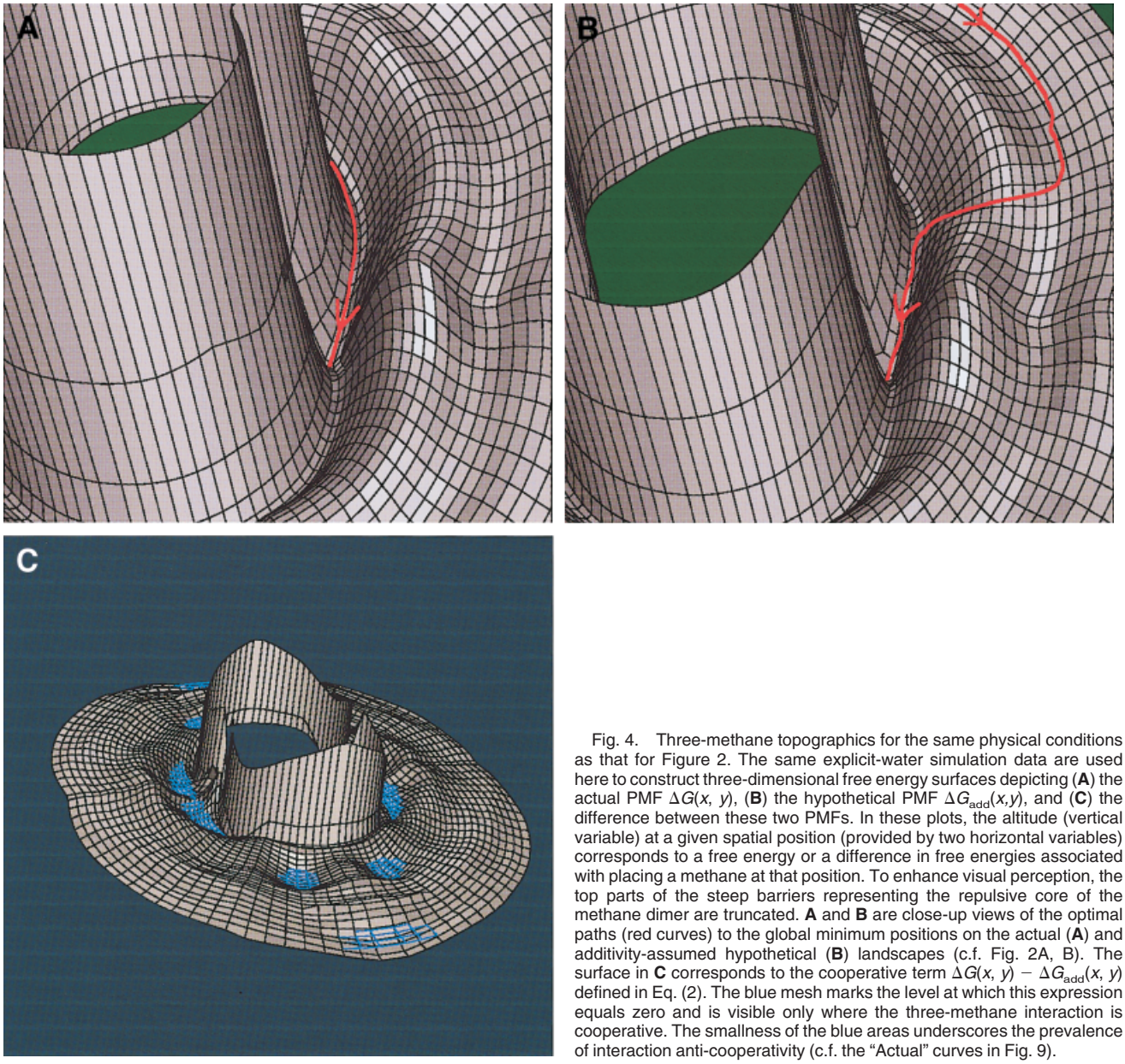

Fig. 4. Three-methane topographics for the same physical conditions as that for Figure 2. The same explicit-water simulation data are used here to construct three-dimensional free energy surfaces depicting (**A**) the actual PMF $\Delta G(x, y)$, (**B**) the hypothetical PMF $\Delta G_{add}(x,y)$, and (**C**) the difference between these two PMFs. In these plots, the altitude (vertical variable) at a given spatial position (provided by two horizontal variables) corresponds to a free energy or a difference in free energies associated with placing a methane at that position. To enhance visual perception, the top parts of the steep barriers representing the repulsive core of the methane dimer are truncated. **A** and **B** are close-up views of the optimal paths (red curves) to the global minimum positions on the actual (**A**) and additivity-assumed hypothetical (**B**) landscapes (c.f. Fig. 2A, B). The surface in **C** corresponds to the cooperative term $\Delta G(x, y) - \Delta G_{add}(x, y)$ defined in Eq. (2). The blue mesh marks the level at which this expression equals zero and is visible only where the three-methane interaction is cooperative. The smallness of the blue areas underscores the prevalence of interaction anti-cooperativity (c.f. the "Actual" curves in Fig. 9).

two-methane desolvation barrier between methane "c" and the approaching single methane (c.f. Fig. 4 in Shimizu and Chan[12]). The present three-methane results show that an accurate account of hydrophobic association kinetics needs to consider the impact of nonadditivity. For instance, if additivity is assumed, the total free energy climb (work done against an opposing mean force) along the optimal path on the actual landscape in Figure 2(A) would be increased (disfavored) by $0.92 - 0.26 = 0.66$ kcal/mol (Fig. 3). These effects for the three-methane system is only of order k_BT (Boltzmann's constant times absolute temperature); therefore, many suboptimal paths are also well populated. Nonetheless, this example shows clearly that hydrophobic nonadditivity has significant effects on the distribution of kinetic paths and suggests strongly that nonadditivity effects on hydrophobic kinetics can be much stronger in protein folding when more and larger hydrophobic groups are involved.

Figure 4 further illustrates the differences between the actual and additivity-assumed hypothetical three-methane free energy landscapes. In particular, the prevalence of interaction anti-cooperativity under ambient conditions is underscored by Figure 4(C), which shows that for the most part, three-methane interaction at 25°C and 1 atm is anti-cooperative and that the interaction is cooperative only for the small areas of the free energy landscape below the light blue mesh.

In general, free energy barriers resulting from multiple-body hydrophobic interactions, such as those encountered above, are of direct relevance to protein folding. Several years ago, Rank and Baker made an insightful suggestion that hydrophobic desolvation barriers may contribute to the rate-

limiting step in folding.[47] However, our recent simulations indicate that the heat capacity signature of the two-methane desolvation barrier is opposite in sign to that determined experimentally for typical folding transition states.[49,50] It follows that the temperature dependencies of protein-folding rates cannot be accounted for by desolvation barriers at the two-methane level.[49] Therefore, heat capacity signatures of many-body desolvation barriers would be needed to elucidate the role of hydrophobic desolvation at the rate-limiting step in folding. But these quantities are yet to be determined because they are costly to compute.

IMPLICIT-WATER EFFECTIVE HYDROPHOBIC POTENTIALS

It would be highly desirable if a simple physical picture could be developed for the seemingly complex phenomena of hydrophobic interactions. This has motivated the formulation of implicit-water (implicit-solvent) models,[71] many of which attempt to account for hydrophobicity in terms of nonpolar surface exposure to water or the nonpolar groups' volumetric effects on the surrounding aqueous environment. These simplified approaches have provided extremely useful insight and are attractive also because they are computationally much more tractable than simulations with (explicit) molecular models of water. However, by construction, implicit-solvent models entail treating water as a continuous medium. Consequently, a certain type of interaction or group additivity is often assumed. This is commonly based on transfer experiments that effectively probe the interactions between solvents (e.g., water or oil) and a single solute,[81] whereby multiple-solute effects are neglected by default. To assess the applicability of these simple methods to protein folding, it is therefore worthwhile to inquire how accurately can implicit-solvent models describe the free energy landscapes of multiple-body hydrophobic interactions. Here we compare the present explicit-water simulated two- and three-methane PMFs against the corresponding predictions from four implicit-solvent models. We begin with a brief summary of the pertinent properties of these models.

Surface Area-Based Approaches (SASA and MSA)

Surface-area approaches assume that hydration effects are proportional to an area measure $\mathcal{A}$ derived from the van der Waals surfaces of the given set of solutes. The most commonly used area measures are the solvent-accessible surface area (SASA)[6,55,58,59,63,64] and the molecular surface area (MSA)[56,57] (Fig. 5). Here SASA is computed by using the software ASC[60] and MSA by MDS.[57] Surface area-based approaches assume that the solvation free energy μ_s is proportional to surface area. Therefore, they predict that the solvation part of the two-methane PMF is given by

$$(\Delta\mu_s^{(2)})_{\mathcal{A}}(\xi) = \gamma(\mathcal{A}_{ab}(\xi) - \mathcal{A}_a - \mathcal{A}_b), \tag{3}$$

where $\mathcal{A}_a$ or $\mathcal{A}_b$ is the surface area (defined by SASA or MSA) of a single methane ("a" or "b"), $\mathcal{A}_{ab}(\xi)$ is the total surface area of two methanes at a distance ξ apart, γ is the free energy per unit area determined by setting the simulated hydration free energy of a single isolated methane $\mu_s^{(1)} = \Delta G^{(1)} = \gamma\mathcal{A}_a$. Similarly, the solvation part of the surface area-predicted three-body PMF is given by

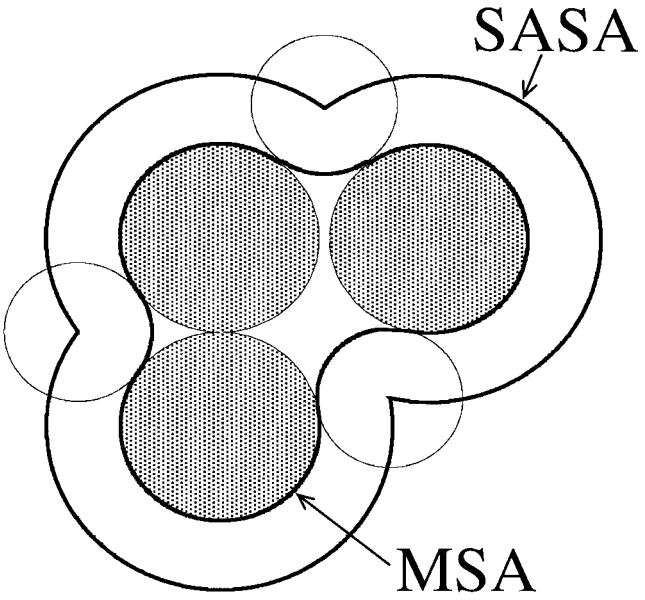

Fig. 5. Definitions of solvent-accessible surface area (SASA)[55] and of molecular surface area (MSA)[56] are illustrated by a configuration of three methanes (shaded circles). Each open circle here is a spherical probe with radius 1.4A representing a water molecule rolling on the van der Waals surface (envelope) of the given three-methane configuration. SASA of the three-methane configuration is traced out by the center of the probe. MSA corresponds to a part of the probe surface facing the three-methane configuration.

$$(\Delta\mu_s^{(3)})_{\mathcal{A}}(\xi,\phi) = \gamma(\mathcal{A}_{abc}(\xi,\phi) - \mathcal{A}_a - \mathcal{A}_{bc}), \tag{4}$$

where $\mathcal{A}_{abc}(\xi, \phi)$ is the total surface area of the three methanes in a ξ, ϕ configuration. In general, surface area prediction for the full PMF is obtained by adding the predicted solvation contributions to the direct interactions among the methanes.

Gaussian Solvent Exclusion Model (L&K)

In addition to surface area-based approaches, we consider also a volume-based implicit-solvent model introduced recently by Lazaridis and Karplus (L&K).[68] This approach has been applied extensively to protein folding.[69,70,82–84] In the L&K prescription, the solvation free energy of a collection of n solutes at positions $\mathbf{r}_i (i = 1, 2, \ldots, n)$ is given by

$$(\mu_s^{(n)})_{L\&K}(\mathbf{r}_1, \mathbf{r}_2, \ldots, \mathbf{r}_n) = n\Delta G^{(1)} - \sum_{i=1}^{n}\sum_{\substack{j=1\\ j\neq i}}^{n}\int_{V_j} d\mathbf{r}_i f_i(r_i), \tag{5}$$

where $\Delta G^{(1)}$ is the hydration free energy of a single solute. The restricted integral $\int_{V_j}$ is only over the volume V_j (defined by the van der Waals radius of solute j, see below), which is excluded from solvent occupation because of the physical presence of solute j. For simplicity, the solutes are taken to be identical in the present analysis. The function f_i is essentially gaussian, viz.,

$$4\pi r_i^2 f_i(r_i) = \frac{2\Delta G^{(1)}}{\sqrt{\pi}\lambda_i} \exp(-x_i^2), \quad (6)$$

where $r_i \equiv |\mathbf{r}_i|, x_i \equiv (r_i - R_i)/\lambda_i, R_i$ is the van der Waals radii of solute i ($= 2^{-5/6} \times$ the collision diameter for a Lennard-Jones sphere), and λ_i is a correlation (decay) length that corresponds to the thickness of one hydration shell ($\lambda_i =$ 3.5 Å is used by L&K for nonpolar groups). A physical interpretation of this approach is that the solvation free energy of a solute resides in the volume of solvent around it, as embodied in the relation $\Delta G^{(1)} = \int d\mathbf{r}_i f_i(r_i)$. Moreover, the importance of the solvent's contribution to $\Delta G^{(1)}$ is expected to decrease with increasing distance from the solute. This trend is controlled by the gaussian decay parameters λ_i in the model.[68] In this model, the only effect of solute j on the solvation free energy of solute i is through volume exclusion, implemented by excluding (subtracting) from the solvation free energy of solute i the part that would otherwise contribute from the volume V_j now occupied by solute j (Eq. 5). This means that, as long as there is no overlap between the van der Waals envelope of a given solute with the van der Waals envelope(s) of a collection of other solutes, the given solute's solvation effects on the other solutes are independent of one another. This is because, by the L&K construction Eq. (5), the combined effect of the given solute in such cases is always the sum of its individual effect on each of the other solutes in the collection.

Equation (5) implies that the solvation part of the two-methane PMF is predicted by L&K to be

$$(\Delta\mu_s^{(2)})_{\mathrm{L\&K}}(\xi) = (\mu_s^{(2)})_{\mathrm{L\&K}}(\xi) - 2\Delta G^{(1)}. \quad (7)$$

The corresponding L&K prediction for the solvation part of the present three-methane PMF is given by

$$(\Delta\mu_s^{(3)})_{\mathrm{L\&K}}(\xi,\phi) = (\mu_s^{(3)})_{\mathrm{L\&K}}(\xi,\phi) - (\mu_s^{(2)})_{\mathrm{L\&K}}(\xi_{bc}) - \Delta G^{(1)}, \quad (8)$$

where ξ_{bc} is the distance between the centers of "b" and "c" in the fixed methane dimer. We adopt the following parameters in the present calculation: $\lambda_i = 3.3$ Å, $R_i = 2.09$ Å, $\Delta G^{(1)} = 2.34$ kcal/mol, and $V_i = 4\pi(R_i)^3/3 = 38.2$ Å^3. The $\Delta G^{(1)}$ value is from our previous simulation that uses $R_i =$ 2.09 Å for methanes (Shimizu and Chan[49]). The value $\lambda_i =$ 3.3 Å is estimated from the position of the first minimum (beyond the first peak) of the methane-water correlation function we simulated. Results presented here for $\lambda_i = 3.3$ Å are practically indistinguishable from the corresponding ones obtained with L&K's[68] $\lambda_i = 3.5$ Å (data for $\lambda_i = 3.5$ Å not shown).

Hydrophobic Force Field (HFF)

All three implicit-solvent models discussed thus far are based on single-solute hydration free energies $\Delta G^{(1)}$. In contrast, the starting point of analysis in the hydrophobic force field (HFF) formulation introduced recently by Hummer is the component two-body PMFs of a given system. Using a systematic expansion that also takes into account cavity formation free energies, HFF provides an approximate description of hydrophobic interactions involving more than two solutes.[67]

In the HFF formulation, the three-methane solvation free energy (i.e., solvation part of the three-body PMF) is given by

$$(\Delta\mu_s^{(3)})_{\mathrm{HFF}}(\xi, \phi) = \frac{1}{2}[\omega^{(2)}(\xi_1) + \omega^{(2)}(\xi_2)] - \bar{\mu}(V_a \cap V_b) - \bar{\mu}(V_a \cap V_c) + \bar{\mu}(V_a \cap V_b \cap V_c). \quad (9)$$

The corresponding HFF prediction for the full PMF is the sum of this solvation contribution and the direct Lennard-Jones interactions among the methanes. A spherical volume of solvent exclusion with radius 3.3 Å is associated with each methane, as in Hummer.[67] Here $V_a \cap V_b$, $V_a \cap V_c$, $V_a \cap V_b \cap V_c$ are the intersection (common) volumes, respectively, of the exclusion spheres of methanes (a, b), (a, c), and (a, b, c). For any given pair of methanes (a, b), the two-body function

$$\omega^{(2)}(\xi) = \Delta\mu_s^{(2)}(\xi) + \bar{\mu}(V_a \cap V_b) \quad (10)$$

is defined by the solvation part $\Delta\mu_s^{(2)}(\xi)$ of a two-methane-like hard-sphere PMF, with a volume term $\bar{\mu}(V_a \cap V_b)$ that ensures[67] $\omega^{(2)}(0) = 0$. The factor of 1/2 in Eq. (9) was introduced by Hummer[67] in an attempt to compensate for the error incurred by truncating the expansion at the pair level. We use the $\bar{\mu}(V)$ and $\omega^{(2)}$ functions deduced by the original author (Figs. 3 and 4 in Hummer[67]) from hard-sphere simulation and information theory considerations.[85] In the present application, because the direct Lennard-Jones model interactions among the methanes are additive, substituting Eqs. (9) and (10) into Eq. (2) leads to an HFF-predicted

$$\text{cooperative term} = -\frac{1}{2}[\omega^{(2)}(\xi_1) + \omega^{(2)}(\xi_2)] + \bar{\mu}(V_a \cap V_b \cap V_c) \quad (11)$$

for the three-methane case.

COMPARING EXPLICIT- AND IMPLICIT-WATER HYDROPHOBIC POTENTIALS

Two-Methane Potential of Mean Force

Figure 6 shows that the depth of the simulated two-methane contact minimum (−0.68 kcal/mol) is best predicted by L&K (−0.51 kcal/mol), although the L&K-predicted contact minimum position at $\xi = 4.1$ Å is slightly shifted relative to the simulated PMF contact minimum position at $\xi = 3.8$ Å. A conspicuous shortcoming of the L&K model is its failure to account for desolvation barriers and solvent-separated minima, as the original authors have noted.[68] SASA also fails on the same counts. This is because both the L&K and SASA formulations for a pair of solutes invariably lead to a monotonic decrease in solvation effects with decreasing solute-solute separation.

On the other hand, MSA predicts a desolvation barrier of +0.08 kcal/mol, which is about one half of the simulated +0.16 kcal/mol. The MSA contact minimum is at −0.39 kcal/mol, which is only about 2/3 as deep as the actual explicit-water simulated minimum. However, despite these discrepancies, aside from the HFF scheme that by construction uses simulated two-body PMFs as the starting point,

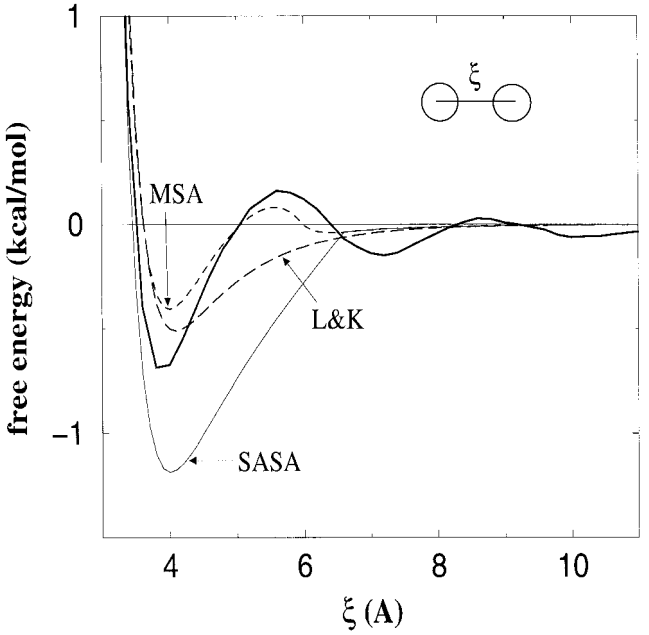

Fig. 6. Comparing two-methane PMF simulated using TIP4P water at 25°C and 1 atm (thick solid curve, c.f. Appendix) with implicit-solvent predictions. The SASA, MSA, and L&K curves correspond to the direct methane-methane Lennard-Jones potential plus, respectively, $(\Delta\mu_s^{(2)})_{\mathscr{A}}$ in Eq. (3) with $\mathscr{A}$ = SASA, MSA, and $(\Delta\mu_s^{(2)})_{\text{L\&K}}$ in Eq. (7). HFF is not included in this comparison because simulated two-body PMFs are used as inputs in the HFF formulation. Note that the definition of the separation variable ξ here for two methanes is different from that in Figs. 1, 7, 9, and 12 for the three-methane system.

MSA is the only implicit-solvent model considered here that exhibits a desolvation barrier for the two-methane PMF.

The two-methane PMF prediction by SASA is much poorer compared to that by MSA, as has been noted before.[46,47,61,62,65,66] The SASA-predicted contact minimum in Figure 6 is at −1.20 kcal/mol, which is almost twice as deep as the simulated value. It should be noted, however, that the accuracy of a given implicit-solvent model can be highly nonuniform depending on the thermodynamic quantities it is applied to predict. For example, for the two-methane case, SASA is inaccurate for PMF, but it is remarkably accurate for predicting the two-methane entropy at contact, although it fails to reproduce the entropy minimum associated with the desolvation free energy barrier.[50] On the other hand, MSA is quite accurate for PMF (Fig. 6), but along with SASA and L&K, it is far from adequate in accounting for the two-methane heat capacity.[50]

Three-Methane Potential of Mean Force

Figure 7 compares the three-methane PMF computed from explicit-water simulation with implicit-solvent predictions for an extended range of configurations. Figure 8 focuses more specifically on the angular dependence of the free energy of association when the single methane is in contact with the methane dimer. Similar to the two-methane case above, L&K quite accurately reproduce the depth of the three-methane contact minima (trench) for the entire angular range. MSA is quantitatively less accurate than L&K in this regard, because the MSA contact trench is shallower. But the MSA-predicted free

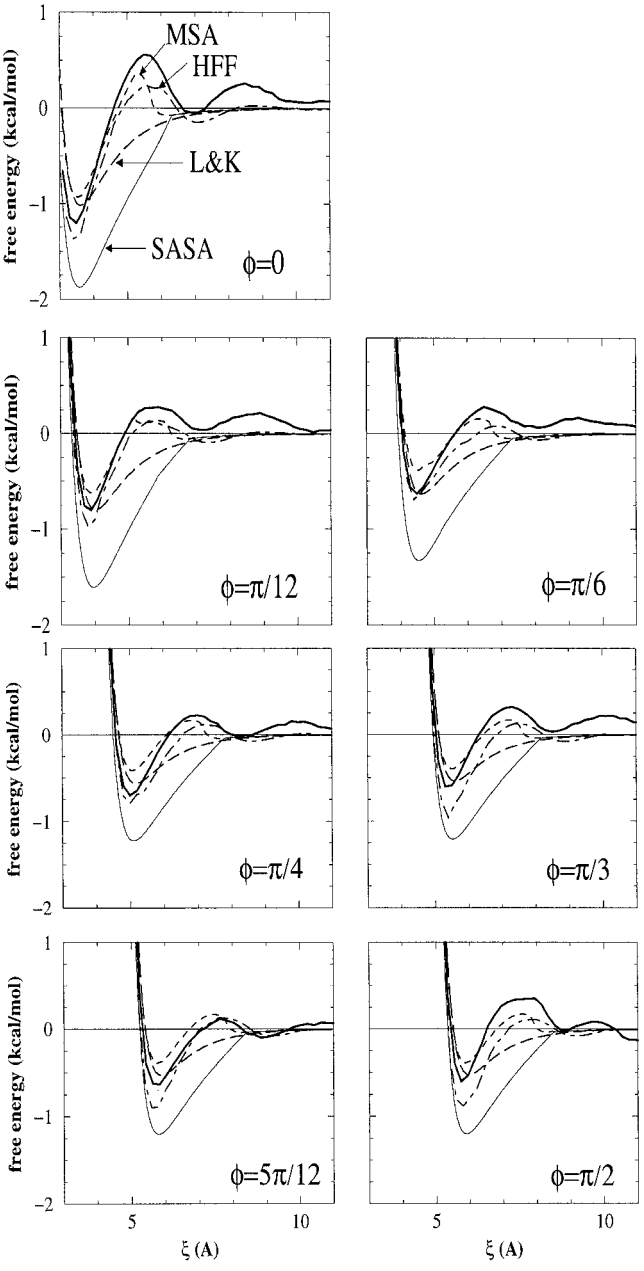

Fig. 7. Three-methane PMFs (thick solid curves) along seven ϕ-directions (c.f. Fig. 1) compared against implict-solvent predictions (line styles defined in the ϕ = 0 panel). The SASA, MSA, L&K, and HFF curves give the direct methane-methane Lennard-Jones interaction plus, respectively, $(\Delta\mu_s^{(3)})_{\mathscr{A}}$ in Eq. (4) with $\mathscr{A}$ = SASA, MSA $(\Delta\mu_s^{(3)})_{\text{L\&K}}$ in Eq. (8), and $(\Delta\mu_s^{(3)})_{\text{HFF}}$ in Eq. (9).

energies for contact positions, nevertheless, follow the same general smooth trend of angular variation as that observed in explicit-water simulation (Fig. 8).

On average, the HFF-predicted free energies for contact positions are closer to the corresponding explicit-water values than MSA. This is remarkable because we do not expect a direct match between the present explicit-water free energies with HFF predictions because the former were obtained by using the TIP4P water model, whereas

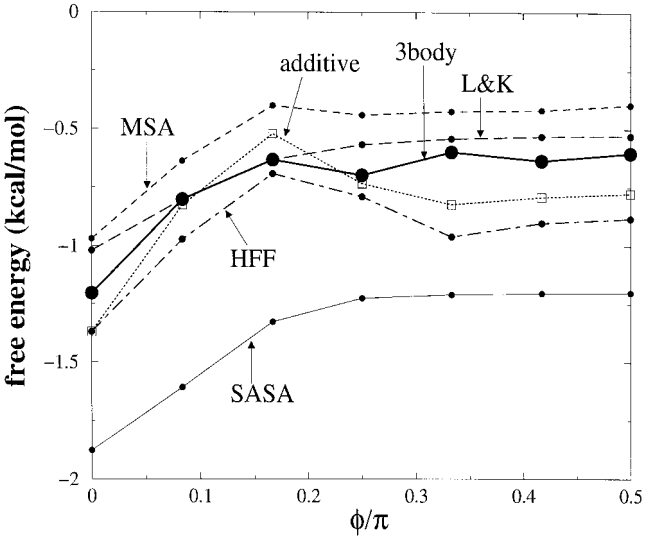

Fig. 8. Angular (ϕ) dependences of the depth of contact free energy trench (deepest minima in Fig. 7). Explicit-water simulation data ("3body," filled circles) are compared with (i) the corresponding hypothetical additivity-assumed values (Eq. 1) based on explicit-water simulated two-methane PMFs ("additive," open squares) and (ii) four implicit-solvent predictions as labeled (c.f. Fig. 7).

the HFF adopted here from the original work were parametrized by using simulation results from the SPC water model.[67] Hence, a comparison between general trends of angular variation may be more pertinent. Figure 8 shows that the ϕ-dependence of HFF-predicted contact free energies exhibits a prominent peak at $\phi = \pi/6$, which is absent on the "3body" curve. In this regard, this HFF prediction matches much better with the hypothetical additivity-assumed profile (labeled "additive") than the actual explicit-water three-methane profile.

Similar to the two-methane case in Figure 6, Figure 7 shows that L&K cannot reproduce the three-methane desolvation peak (which may be more appropriately referred as a "desolvation ridge" with a ϕ-dependence). Instead, the L&K free energy of association decreases monotonically with decreasing separation ξ throughout the desolvation ridge region. On the other hand, both MSA and HFF exhibit a desolvation barrier and a weak solvent-separated trench. In this particular comparison, the MSA-predicted height of the desolvation ridge comes closest to the explicit-water result.

Among the implicit-solvent models tested, SASA's result is the most unsatisfactory in terms of reproducing three-methane free energies. SASA does not predict any desolvation ridge. The SASA prediction of the depth of contact trench is on average almost twice as deep as that from explicit-water simulation. Considering the results in Figures 6–8 as a whole, it is quite clear that SASA grossly overestimates the favorability of hydrophobic association among a small number of methane-like solutes.

Nonadditive Interactions: Anti-Cooperativity and Cooperativity

Figure 9 compares the explicit-water prediction of three-methane interaction nonadditivity with corresponding implicit-water predictions. As noted before[50] [c.f. Fig. 4(C)], results from explicit-water TIP4P simulation indicate that interaction anti-cooperativity is prevalence under ambient conditions. Among the implicit-water models, L&K predict strict interaction additivity for essentially all configurations considered except when the van der Waals envelope of the single methane "a" overlaps with that of either of the

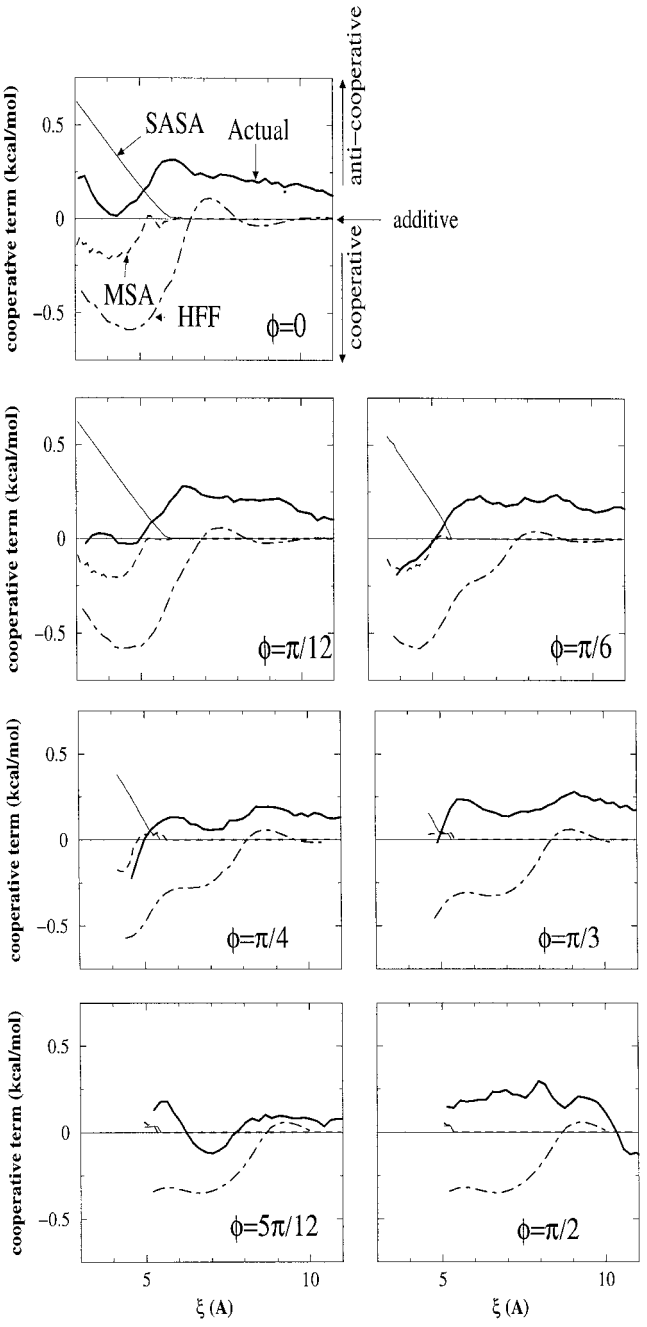

Fig. 9. The cooperative term (Eq. 2) along seven ϕ-directions (c.f. Fig. 1). Explicit-water simulated data (labeled "Actual") is compared against implicit-solvent predictions. (Line styles defined in the $\phi = 0$ panel.) The HFF cooperative term is given by Eq. 11. The cooperative term for L&K (not shown) is zero for essentially all configurations (i.e., those with $\xi_1, \xi_2 \geq 2R_i = 4.2$A; see text).

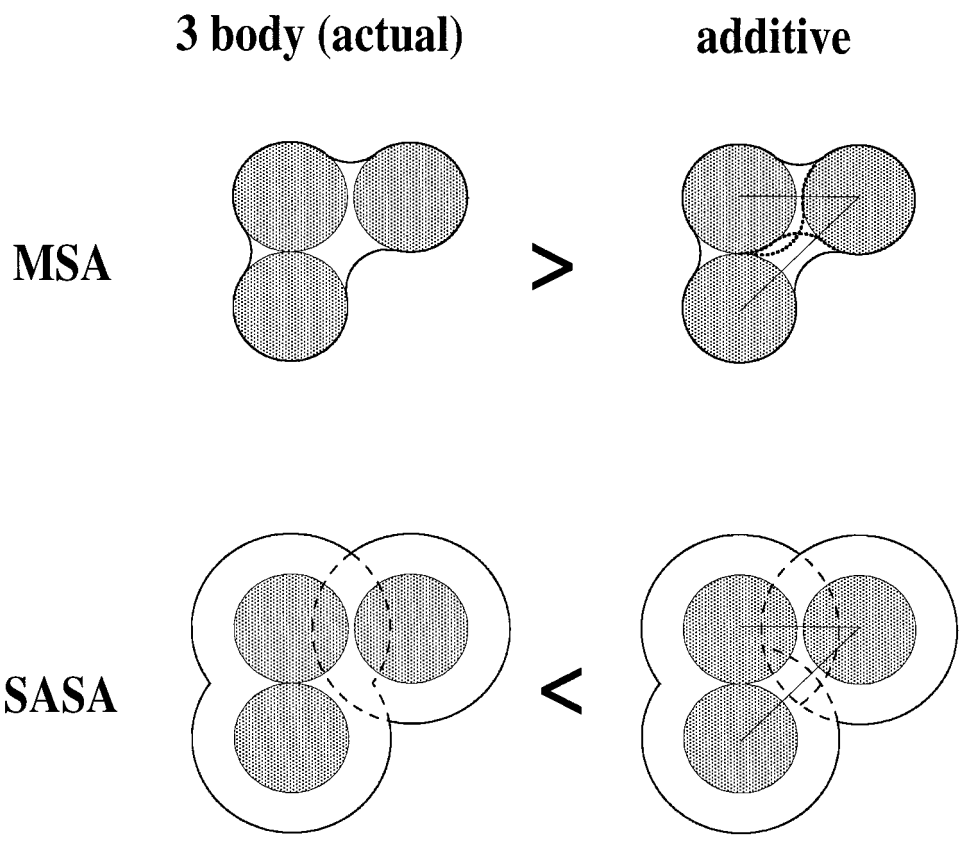

Fig. 10. A schematic account of interaction cooperativity and anti-cooperativity in two surface area-based implicit-solvent models. The ">" and "<" refer to the total surface area buried (MSA or SASA) on association of the single methane and the methane dimer (c.f. Fig. 5), which is taken to be proportional to the change in hydration free energy (Eq. 4). Additivity considerations are applied to the two methane pairs, indicated by thin straight lines joining the centers of each pair. **Top:** MSA predicts cooperativity because the actual MSA buried (left) by three-body association is more than the pairwise sum of MSA buried, because the saddle surfaces (dotted curves on the right) inside the overall MSA envelope are considered to be exposed (not buried) in the pairwise sum. A similar argument regarding MSA was advanced by Czaplewski et al.[46] **Bottom:** SASA predicts anti-cooperativity because the SASA buried (dashed curves) for the actual interaction (left) is less than the pairwise sum of SASA buried (right).

two methanes in the "b, c" dimer (see above). Figure 9 shows that none of the implicit-water models tested reproduces well the pattern of nonadditivity obtained from explicit-water simulation.

A prominent feature in Figure 9 is that for $\phi < \pi/4$, significant anti-cooperativity is predicted by SASA, whereas cooperativity is predicted by MSA when the single methane and the methane dimer is in relatively close proximity ($\xi < 5.5$ Å). These opposing properties of MSA and SASA are readily elucidated by geometrical considerations (Fig. 10). In contrast to the explicit-water prediction of significant anti-cooperativity for all ϕ's, nonadditivity essentially disappears according to both MSA and SASA when $\phi \geq \pi/3$ (Fig. 9). This is because for large ϕ's the single methane ("a" in Fig. 1) can affect only the surface measure of one of the methanes in the dimer (methane "b"). This implies that surface area-based models in general miss spatially long-range hydration effects. Figure 9 also indicates that HFF predicts strong cooperative effects of ≈ -0.3 to -0.5 kcal/mol for the entire contact trench, much stronger than that predicted by MSA. However, a cooperative effect at the contact trench is opposite to the anti-cooperativity observed in explicit-water simulation for these three-methane configurations.

The comparisons in Figures 7 and 8 show that HFF is much superior to SASA in accounting for multiple-body nonpolar hydration free energies. HFF is also superior to L&K in that desolvation barriers are predicted by HFF but not L&K, although L&K appears to be more accurate for the contact trench. However, HFF appears to fare slightly worse than MSA (which also predicts desolvation barriers) with regard to nonadditivity properties, at least at the three-methane level considered here. In particular, the kinetic consequences of the discrepancy between the HFF-predicted and the explicit-water free energy profiles of the contact trench may be significant (c.f. Figs. 2–4).

IMPLICATIONS OF INTERACTION NONADDITIVITY ON PROTEIN THERMODYNAMICS: AN EXAMPLE

A main motivation for investigating multiple-body hydrophobic interactions is to gain a better understanding of

protein energetics.[12,13,44–47,49,50] Here we explore one of many potentially far-reaching ramifications of hydrophobic nonadditivity on protein folding. As an illustrative example, new features are introduced to augment a highly simplified protein chain model[13] to partly capture the physics of interaction nonadditivity. Self-contained polymer models of proteins[86] are indispensable in our endeavor. This is because in their absence the implications of simulated interactions among disconnected solutes on chain properties are often not obvious.[13,44] Based on chain model analyses, our group has previously argued[23,24] that if hydrophobic interactions were additive, they would not be sufficient to account for calorimetric two-state cooperativity. This property is characterized by a van't Hoff to calorimetric enthalpy ratio $\Delta H_{\rm vH}/\Delta H_{\rm cal} \approx 1$ and has been observed experimentally for many small proteins.[6] Now, it is natural to ask: How would hydrophobic nonadditivity affect this outlook? Figure 11 addresses this question by a simple protein chain model. The aim of this schematic calculation is to explore the basic principles governing the effects of different types of nonadditivity on chain thermodynamics. For this purpose, in this section only the general trend—but not the quantitative details—of the simulated free energies are exploited.

Explicit-water simulation data indicates that three-methane hydrophobic interactions are largely anti-cooperative at 25°C and 1 atm. The maximum anti-cooperative effect is approximately +0.3 kcal/mol (Fig. 9). Our recent analysis of close-packed methane clusters suggests further that under the same ambient conditions, anti-cooperativity may increase with cluster size, because anti-cooperativity is determined to be of order +1.0 kcal/mol per methane in the limit of an infinite methane cluster.[12] (The corresponding estimate using the present two-methane PMF in the Appendix is very similar.) The upper panel of Figure 11 first compares the additive case to an anti-cooperative scenario under the simplifying condition that the hydrophobic interactions in the model are temperature independent. In that case, the heat capacity of the model protein is given by the standard relation

$$C_P(T) = \frac{\langle H_c^2(T)\rangle_c - \langle H_c(T)\rangle_c^2}{k_B T^2}, \qquad (12)$$

where $\langle \ldots \rangle_c$ denotes Boltzmann averaging over chain conformations. The enthalpy H_c for a given chain conformation with h hydrophobic contacts is $H_c = h\varepsilon$ for this additive case. For the anti-cooperative example, we classify hydrophobic contacts into (1) exposed, (2) partially buried, and (3) fully buried (see Fig. 11). The enthalpy of a conformation is then given by $H_c = \Sigma_i h_i \varepsilon_i$, where h_i values are the numbers of the three types of hydrophobic contacts (i = 1, 2, 3) in the given conformation. All heat capacity scans in Figure 11 are determined from the exactly enumerated number of conformations as a function of h or the h_i values.

As shown before,[23] the additive case with a T-independent ε is not calorimetrically two-state. Its $\Delta H_{\rm vH}/\Delta H_{\rm cal}$ ratio κ_2 without empirical baseline subtractions is 0.54 (as in Chan[23]). Even after baseline subtractions, the ratio $\kappa_2^{(s)}$ is only 0.70, far from the proteinlike requirement of ≈ 1.

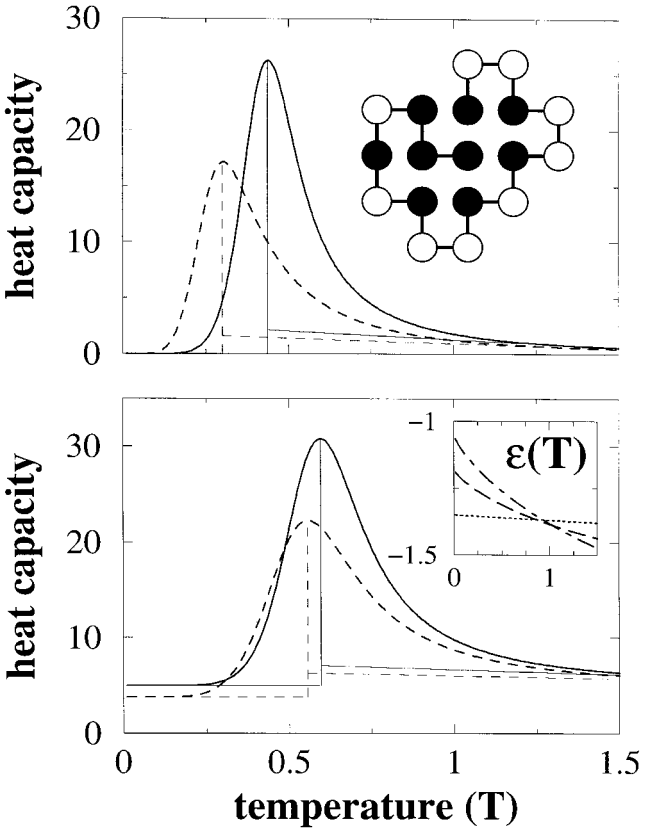

Fig. 11. A simple illustration of how nonadditive and temperature-dependent effective intrachain interactions may affect a protein's calorimetric cooperativity. The model heat capacity scans plotted are based on the two-dimensional lattice hydrophobic-polar (HP) sequence in Figure 2 of Chan,[23] shown here in its ground-state conformation (top: H: black beads; P: white beads). This is the conformation with the lowest free energy for every interaction scheme in the temperature range considered in this figure. The model heat capacity values should be viewed as relative, to allow for a possible "buffer" contribution.[23,24] By using the same modeling procedure as before,[25] the van't Hoff to calorimetric enthalpy ratio $\Delta H_{\rm vH}/\Delta H_{\rm cal} = \kappa_2$ (without empirical native/denatured baseline subtractions) and $\kappa_2^{(s)}$ (with native/denatured baseline subtractions) are computed[24] from the heat capacity scans. Temperature is in units of $1/k_B$. **Top:** Temperature-independent interactions (Eq. 12). The solid scan is for the additive case,[23] in which each hydrophobic-hydrophobic (HH) contact is assigned the same T-independent contact free energy (enthalpy) $\varepsilon = -1$ (c.f. Fig. 4 in Chan[23]). The dashed scan is for an anti-cooperative case in which exposed, partially buried, and fully buried HH contacts are decreasingly favorable, with $\varepsilon_i = -1.0$, -0.9, and -0.75, respectively. In the present treatment, an HH contact is exposed if two or more of the combined surfaces of the pair of H monomers in contact are exposed (i.e., not contacting other H or P monomers). (Note that each individual monomer not at the chain ends has two surfaces; a monomer at the chain ends has three surfaces.) An HH contact is partially buried or fully buried if, respectively, one or none of the combined surfaces of the contacting HH pair is exposed. **Bottom:** Temperature-dependent interactions [Eq. (14). The solid heat capacity scan is for an additive case in which each HH contributes a T-dependent free energy $\varepsilon(T)$. The heat capacity values are obtained by using the $\varepsilon(T)$ given by the dotted line in the inset. The dashed heat capacity scan is for an nonadditive example, in which the $\varepsilon_i(T)$ values for exposed, partially buried, and fully buried HH contacts (defined as above) are assigned, respectively, by the dotted, dashed, and dashed-dotted curves in the inset. See text for further details.

Here interaction anti-cooperativity makes the model even less protein-like, leading to even lower $\Delta H_{\rm vH}/\Delta H_{\rm cal}$ ratios. For the anti-cooperative example in the upper panel of Figure 11, κ_2, $\kappa_2^{(s)}$ = 0.39, 0.53.

The lower panel of Figure 11 takes into account that hydrophobic interactions are temperature dependent,[2,3,6,49] an effect arising from averaging over solvent degrees of freedom. In general, the total heat capacity of a chain-in-solvent system is given by

$$C_{P,\mathrm{total}}(T) = \left(\frac{\partial \langle H\rangle_{\mathrm{total}}}{\partial T}\right)_P = \left(\frac{\partial \langle\langle H\rangle_{s}\rangle_{c}}{\partial T}\right)_P, \qquad (13)$$

where the enthalpy $H = H(\{s\}, \{c\})$ of the entire system is in general a function of both the solvent ($\{s\}$) and chain conformational ($\{c\}$) degrees of freedom. The second equality holds because the global Boltzmann average $\langle \ldots \rangle_{\mathrm{total}}$ over all configurations can clearly be performed by first averaging over solvent configurations ($\langle \ldots \rangle_s$) and then over chain conformations ($\langle \ldots \rangle_c$), because the averaging integrals over different degrees of freedom can be performed in any order. A straightforward statistical mechanical analysis of this relation leads to the formula

$$C_{P,\mathrm{total}}(T) = \frac{\langle H_c^2(T)\rangle_c - \langle H_c(T)\rangle_c^2}{k_B T^2} + \langle C_{P,c}(T)\rangle_c, \qquad (14)$$

where $H_c(T) \equiv \langle H(\{s\}, \{c\})\rangle_s$ and $C_{P,c}(T) \equiv [\partial H_c(T)/\partial T]_P$ are the enthalpy and heat capacity of a given conformation.

In the lower panel of Figure 11, a T-dependent contact free energy $\varepsilon(T)$ is used for the additive case, and three T-dependent contact free energies $\varepsilon_i(T)$ are used for the nonadditive example. The corresponding enthalpy of a given conformation is $H_c(T) = -hT^2\{\partial[\varepsilon(T)/T]/\partial T\}$ and $H_c(T) = -\Sigma_i h_i T^2\{\partial[\varepsilon_i(T)/T]/\partial T\}$, respectively. The nonadditive example here is partly motivated by the fact that although hydrophobic interactions appear to be predominantly anti-cooperative under ambient conditions, they seem to be more cooperative at higher temperatures. This is because the simulation data we obtained for 95°C and 1 atm indicate that the formation of an infinite close-packed methane cluster at 95°C is cooperative by ≈ -1.5 kcal/mol per methane instead of anti-cooperative by $\approx +1.1$ kcal/mol per methane at 25°C (see above). Here this temperature dependence of nonadditivity is qualitatively analyzed by having an exposed $\varepsilon_i(T)$, which is more favorable (more negative) than the partially and fully buried $\varepsilon_i(T)$ values for low temperatures and a reversed trend for high temperatures (Fig. 11, lower panel inset). A shift of the denatured (high-T) baseline relative to the native (low-T) baseline is expected for the present nonadditive example because a positive heat capacity is associated with some of the contact free energies (nonlinear curves in the inset). Hence, it is only appropriate to compute the $\Delta H_{\mathrm{vH}}/\Delta H_{\mathrm{cal}}$ ratio $\kappa_2^{(s)}$ with empirical baseline subtractions. Neither the additive case ($\kappa_2^{(s)} = 0.7$) nor the nonadditive example ($\kappa_2^{(s)} = 0.67$) here satisfies the calorimetric criterion.

The overall message of Figure 11 is that the trend of hydrophobic nonadditivity observed in our explicit-water simulation is not likely to improve, relative to the hypothetical additive case, the thermodynamic cooperativity of folding/unfolding transitions of heteropolymers with hydrophobic interactions. The additive case is far from being calorimetrically two-state to begin with.[23] Therefore, the present results strongly suggest that hydrophobic interactions alone are insufficient to account for the calorimetric two-state cooperativity in real proteins.

CONCLUSIONS

A prerequisite for tackling hydrophobic nonadditivity is a means to appropriately compare multiple-body interactions involving different numbers of nonpolar solutes. Here a general test-particle technique that ensures meaningful comparisons of PMFs is applied to analyze extensive simulation data obtained from the TIP4P model of water. This effort represents only an initial step toward unraveling of the complex microscopic nonadditivity effects in hydrophobic interactions and their impact on protein folding. Clearly, the robustness and generality of our results should be ascertained by seeking a deeper understanding of the physics of hydrophobic nonadditivity in terms of the underlying water structures (c.f. Appendix) and by further testing using other water models[87,88] and more extensive simulations.

Systematic PMF comparisons indicate that multiple-body thermodynamic and kinetic effects are significant in hydrophobic interactions, which are found to be anti-cooperative under ambient conditions for most of the three-methane configurations investigated here and for the formation of (infinitely) large close-packed methane clusters in water.[12] This suggests strongly that other driving forces in addition to nonspecific hydrophobic interactions must contribute to the physics of thermodynamic cooperativity of protein folding/unfolding transitions,[23–25] as illustrated schematically in the last section by the heat capacity scans of a simple lattice chain model. Further complexities revealed by our TIP4P simulation include a significant temperature dependence of hydrophobic nonadditivity (details not shown), the full implication of which on protein conformational distributions remains to be explored.

The present analysis provides directions for how implicit-solvent (implicit-water) treatments of protein hydrophobic interactions may be improved. Comparisons of explicit-water results with implicit-water predictions indicate that the strengths and weaknesses of different implicit-water models vary. Success in modeling the behavior of one thermodynamic signature does not guarantee success in modeling others. A case in point is that although MSA, SASA, and L&K have various degrees of success and failure in predicting two- and three-methane free energies (see above) and two-methane entropy,[50] none of them is adequate in accounting for a dramatic non-monotonic spatial dependence of two-methane heat capacity observed in explicit-water simulation.[50] (Note that the current formulation of HFF is only for free energies.) But such a spatial dependence of heat capacity of hydrophobic association is likely to be of critical importance in reconciling calorimetric data and the experimental observation of compact protein denatured states,[50,69,89–93] as we have recently commented.[50] This implies that, to develop better implicit-solvent models, it would be necessary to adopt distinct spatial dependencies for different thermodynamic quantities such as free energy, entropy, and heat capacity.

NOTE ADDED IN PROOF

After the present article has been accepted for publication, a study by Czaplewski et al.[105] on hydrophobic nonadditivity and implicit solvent models appeared, some conclusions of which are different from ours. In particular, using prescriptions similar to that in Ref. 46, a cooperative effect was predicted for three methanes in close association. For the reasons detailed in Refs. 12, 94, and the Appendix of the present article, we do not agree with this conclusion in Ref. 105. The issues raised in the authors' prior commentary[95] about zero PMF value determination and the differences between Refs. 12 and 46 with regard to the sign of nonadditivity were not addressed in Ref. 105.

ACKNOWLEDGMENTS

We dedicate this work to the memory of Peter A. Kollman, who passed away while this report was in preparation. We are grateful to Frank Eisenhaber for his generous help with the program ASC. We thank Angel Garcia and Benoit Roux for helpful discussions, Danny Heap for his effort in maintaining our computing system, Hüseyin Kaya for his assistance in making some of the figures, and two anonymous referees for very useful comments. This work was supported in part by the Connaught Fund, a Premier's Research Excellence Award from the Province of Ontario, and Medical Research Council of Canada grant no. MT-15323. H.S.C. is a Canada Research Chair in Biochemistry.

APPENDIX: ACCURACY OF TWO-METHANE PMF AND THREE-METHANE NONADDITIVITY

Here we address the reliability and significance of the nonadditivity effects reported above. For this purpose, one has to ensure that in the test-particle insertion method used here, the single-, two-, and three-methane chemical potentials are all sufficiently accurate. Since our previous reports,[12,49] we have improved the reliability of our simulated single- and two-methane free energies by more extensive sampling. Based on data collected over 6×10^6 Monte Carlo passes and a comparison between half-simulation and full-simulation results, the hydration Gibbs free energy of a single methane is determined to be 2.326 ± 0.006 kcal/mol at 25°C and 1 atm. This new result is consistent with our previous result of 2.34 ± 0.05 kcal/mol (averaged over 2×10^6 passes).[49] Similarly, we have improved the reliability of the two-methane PMF at 25°C and 1 atm by using approximately 7 times the number of Monte Carlo passes used in our previous investigations.[12,49,94] The new additivity-assumed PMF in Figure 12 as well as all of the analyses in the main text are based on this new two-methane PMF, with improved reliability of $\pm$ 0.02 kcal/mol except in narrow regions around methane-methane separations of 5.0 and 8.2 Å, where the uncertainties are approximately ± 0.035 kcal/mol. For all methane-methane separations at the contact minimum and larger, the new two-methane PMF (full-simulation average) is within ± 0.05 kcal/mol of our previously reported two-methane PMF at 25°C and 1 atm.[12,49,94]

The nonadditivity effects in Figure 12 are in essential agreement with that in Figure 2 of our original report.[12]

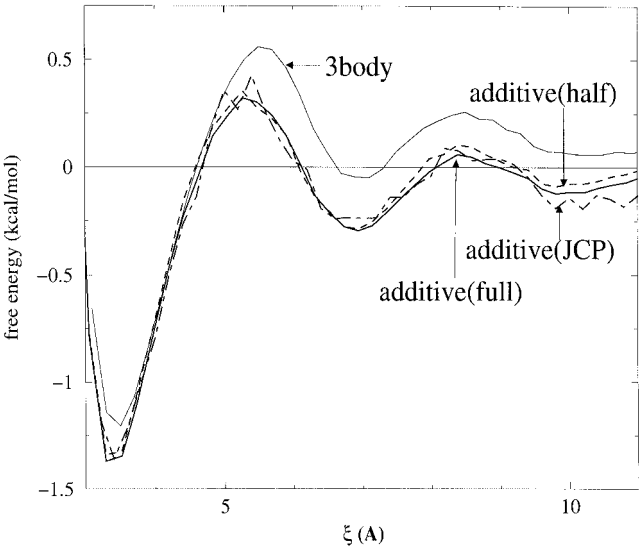

Fig. 12. Three-methane PMF at 25°C and 1 atm for bringing a single methane from infinity ($\xi \to \infty$) along a $\phi = 0$ direction to a finite distance ξ apart from the fixed methane dimer (solid "3body" curve, from Fig. 2 of Shimizu and Chan[12]) is compared against additivity-assumed hypothetical PMFs (ΔG_{add}, Eq. 1) from two separate simulations using the test-particle method. The two-methane PMF under the same conditions (dashed curve) labeled "additive (JCP)" is from our previous work,[12,49] which was obtained by averaging over 8.8×10^6 passes. The thick solid curve labeled "additive (full)" is the two-methane PMF newly obtained by averaging over 6.2×10^7 passes. The accuracy of this PMF is assessed by comparing the full-simulation result with its corresponding half-simulation result (dashed curve labeled "additive (half)," averaged over 3.1×10^7 passes).

The cooperative term in Eq. (2) contains one factor each of the single- and three-methane chemical potentials and two factors of the two-methane chemical potentials.[49,95] Therefore, based on the above error estimates, the uncertainty of the cooperative term in the present work is approximately $0.005 + 2 \times 0.02 + 0.006 = 0.051$ kcal/mol. This error estimate is much smaller than the anti-cooperative effect of approximately 0.2 kcal/mol for $\xi \approx 5.5$–11.0 Å in Figure 12, indicating strongly that the anti-cooperative effect observed at the contact minimum and in the region encompassing the desolvation barrier and the first solvent-separated minimum is reliable.[‡]

In our simulations,[49] the cutoff distance of water-water and water-methane interactions is 9.0 Å. Ewald summation is not used because the TIP4P water model[96] was thermodynamically parametrized by using cutoffs for electrostatic interactions without Ewald summations. This fact has recently been noted by Czaplewski et al., who report that introducing Ewald summations in their simulations does not affect two-methane PMF values beyond sampling uncertainties.[46] Cutoffs of electrostatic interactions without Ewald summations have also been used in several other PMF studies.[47,48,87,97–100] Moreover, our

[‡]The smaller error estimate for our three-methane PMF[12] (± 0.005 kcal/mol) relative to that for the present two-methane PMF (± 0.02 kcal/mol) is partly due to enhanced statistics resulting from a higher frequency of snapshot recording we have used in the computation of the three-methane PMF (every 10 passes) than that of the two-methane PMF (every 100 passes).

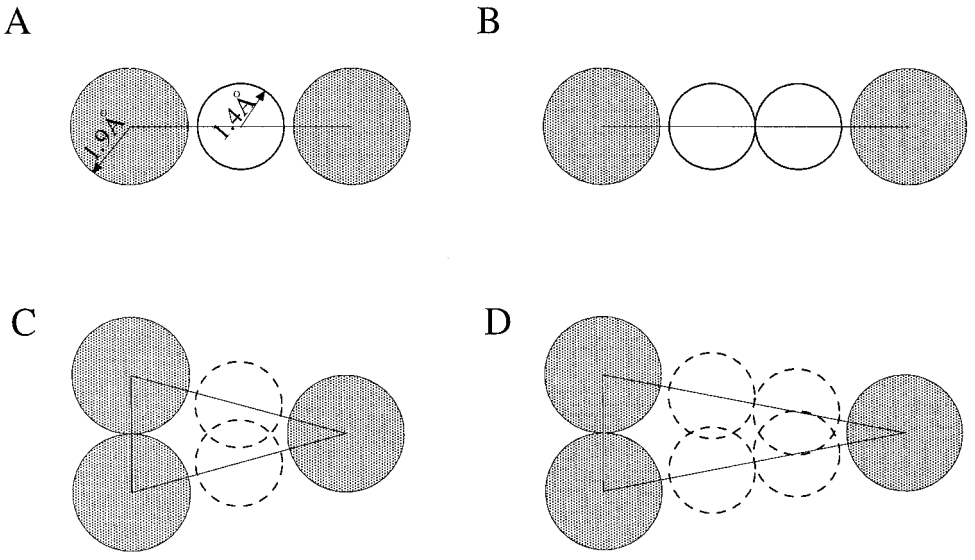

Fig. 13. Hydrophobic nonadditivity. Methanes and water molecules are schematically shown as shaded and open circles respectively (c.f. Fig. 5). **A, B:** Two possible methane-water-methane configurations when the methane pairs are solvent separated. In (**C,D**), the distances between the single methane and each of the methanes of the dimer are respectively identical to that in (**A**) and (**B**). Parts (**C**) and (**D**) show the impossibility of (additively) superposing the methane-water-methane configurations in (**A**) and (**B**) for the interaction between a methane dimer and a third methane.

predicted entropy of two-methane association[49,50] agrees closely with that from a recent independent study[102] that uses the Ewald method.

A major advantage of the test-particle insertion method we have used is that it does not rely on *a priori* assumptions about the spatial range of hydrophobic nonadditivity.[12,94] For simulations of comparable sizes, the test-particle insertion method offers a more reliable determination of the zero-PMF baseline because zero PMF value is ascertained by the free energy of insertion of a single methane in a simulation box of pure water. Such an inserted methane is effectively much more isolated (and therefore allows for a physically more accurate determination of zero PMF) than methanes in other methods of zero-PMF baseline determination that rely on assumptions about the behavior of the interaction free energy between methanes separated by finite distances in the same simulation box.[12,94] Moreover, in the test-particle insertion method, the PMF value at every spatial separation is computed independently. Therefore, even in the event that PMF accuracy is compromised at large separations due to the proximity of methanes (in the simulation box) to image methanes in neighboring periodic boxes,[§] the accuracy of PMF values at smaller separations should be much less affected.[94,95] The linear dimension of our simulation box is ≈23 Å. In view of potential artifacts arising from periodic boundary conditions, our conclusions are only drawn from data for $\xi \leq 11.0$ Å.

As discussed in the main text, implicit-solvent models of hydrophobic interactions often treat water as a continuous medium. Consequently, important nonadditive features are missed. Figure 13 shows that even simple considerations of discrete water molecules lead one to expect nonadditivity effects because it is geometrically impossible to superpose certain water/methane pair configurations when three methanes are involved (an "excluded volume" effect). Under ambient conditions, water molecules in the vicinity of nonpolar solutes exhibit orientational preferences due to "clathrate-like" arrangements, even though structural rigidity is lacking.[102,103] It is highly unlikely that the orientational preferences of water molecules around a pair of isolated nonpolar solutes can be maintained when the solute pair is part of a larger number of closely associated nonpolar solutes. Because the orientational probability of a water molecule around a group of nonpolar solutes does not equal the product of corresponding orientational probabilities for the constituent pairs of isolated nonpolar solutes, hydrophobic nonadditivity is expected.

Figure 13 provides further rationalization for nonadditivity effects to have significantly longer spatial ranges than that predicted by common implicit-solvent surface areas models, as shown by the simulation results in Figure 9. Indeed, Figure 13 indicates that additivity of hydrophobic interaction is unlikely for the three-methane configuration in Figure 13C, D (with $\xi = 6.7$ Å and 9.8 Å, respectively; c.f. Fig. 1). This is noteworthy because it has been assumed[46,95] that three-methane hydrophobic interaction is

[§]This means that although the non-zero PMF values at $\xi = 11.0$ Å in Figure 12 may reflect that the physical ranges of solvent-mediated interactions studied are larger than $\xi = 11.0$ Å, artifacts from periodic boundary conditions may also contribute to PMF values at these relatively large separations in our simulations. Clearly, the spatial range of solvent-mediated two-methane interactions should be finite, so the PMF is expected to ultimately decay to zero. The test-particle method allows for the calculation of *absolute* PMFs. Thus, non-zero PMF values in the present test-particle analysis imply that much larger simulation boxes will be needed to exhaust the effective spatial range of two-methane hydrophobic interactions. This question remains to be addressed.

approximately additive around $\xi = 7.26-8.28$ Å. The range of hydrophobic interactions can be extended.[104] The simple geometrical consideration in Figure 13 and the simulation data in the present work argue against[12,94] this and other *ad hoc* assumptions[105] about the spatial range of hydrophobic nonadditivity.

REFERENCES

1. Kauzmann W. Some factors in the interpretation of protein denaturation. Adv Protein Chem 1959;14:1–63.
2. Tanford C. Protein denaturation. Adv Protein Chem 1968;23:121–282.
3. Dill KA. Dominant forces in protein folding. Biochemistry 1990; 29:7133–7155.
4. Honig B, Yang AS. Free energy balance in protein folding. Adv Protein Chem 1995;46:27–58.
5. Lazaridis T, Archontis G, Karplus M. Enthalphic contribution to protein stability: insights from atom-based calculations and statistical mechanics. Adv Protein Chem 1995;47:231–306.
6. Makhatadze GI, Privalov PL. Energetics of protein structure. Adv Protein Chem 1995;47:307–425.
7. Hummer G, Garde S, García AE, Paulaitis ME, Pratt LR. Hydrophobic effects on a molecular scale. J Phys Chem B 1998;102:10469–10482.
8. Sorenson JM, Hura G, Soper AK, Pertsemlidis A, Head-Gordon T. Determining the role of hydration forces in protein folding. J Phys Chem B 1999;103:5413–5426.
9. Huang DM, Chandler D. Temperature and length scale dependence of hydrophobic effects and their possible implications for protein folding. Proc Natl Acad Sci USA 2000;97:8324–8327.
10. Pace CN, Shirley BA, McNutt M, Gajiwala K. Forces contributing to the conformational stability of proteins. FASEB J 1996;76:75–83.
11. Pace CN. Polar group burial contributes more to protein stability than nonpolar group burial. Biochemistry 2001;40:310–313.
12. Shimizu S, Chan HS. Anti-cooperativity in hydrophobic interactions: a simulation study of spatial dependence of three-body effects and beyond. J Chem Phys 2001;115:1414–1421.
13. Shimizu S, Chan HS. Statistical mechanics of solvophobic aggregation: additive and cooperative effects. J Chem Phys 2001;115: 3424–3431.
14. Cantor CR, Schimmel PR. Biophysical Chemistry. New York: W. H. Freeman & Company; 1980.
15. Mark AE, van Gunsteren WF. Decomposition of the free-energy of a system in terms of specific interactions—implications for theoretical and experimental studies. J Mol Biol 1994;240:167–176.
16. Dill KA. Additivity principles in biochemistry. J Biol Chem 1997;272:701–704.
17. Martorana V, Bulone D, San Biagio PL, Palma-Vittorelli MB, Palma MU. Collective properties of hydration: long range and specificity of hydrophobic interactions. Biophys J 1997;73:31–37.
18. Martorana V, Corongiu G, Palma MU. Interaction of explicit solvent with hydrophobic/philic/charged residues of a protein: residue character vs. conformational context. Proteins 1998;32: 129–135.
19. San Biagio PL, Martorana V, Bulone D, Palma-Vittorelli MB, Palma MU. Solvent-induced free energy landscape and solute-solvent dynamic coupling in a multielement solute. Biophys J 1999;77:2470–2478.
20. Chan HS, Dill KA. Comparing folding codes for proteins and polymers. Proteins 1996;24:335–344.
21. Wolynes PG. As simple as can be? Nat Struct Biol 1997;4:871–874.
22. Chan HS. Folding alphabets. Nat Struct Biol 1999;6:994–996.
23. Chan HS. Modeling protein density of states: additive hydrophobic effects are insufficient for calorimetric two-state cooperativity. Proteins 2000;40:543–571.
24. Kaya H, Chan HS. Polymer principles of protein calorimetric two-state cooperativity. Proteins 2000;40:637–661. [Erratum: Proteins 2001;43:523.]
25. Kaya H, Chan HS. Energetic components of cooperative protein folding. Phys Rev Lett 2000;85:4823–4826.
26. Kaya H, Chan HS. Towards a consistent modeling of protein thermodynamic and kinetic cooperativity: how applicable is the transition state picture to folding and unfolding? J Mol Biol 2002;315:899–909.
27. Chan HS. Protein folding: matching speed and locality. Nature 1998;392:761–763.
28. Kolinski A, Galazka W, Skolnick J. On the origin of the cooperativity of protein folding: implications from model simulations. Proteins 1996;26:271–287.
29. Hao M-H, Scheraga HA. Characterization of foldable protein models: thermodynamics, folding kinetics and force field. J Chem Phys 1997;107:8089–8102.
30. Takada S, Luthey-Schulten Z, Wolynes PG. Folding dynamics with nonadditive forces: a simulation study of a designed helical protein and a random heteropolymer. J Chem Phys 1999;110: 11616–11629.
31. Eastwood MP, Wolynes PG. Role of explicity cooperative interactions in protein folding funnels: a simulation study. J Chem Phys 2001;114:4702–4716.
32. Tanaka S, Scheraga HA. Medium- and long-range interaction parameters between amino acids for predicting three-dimensional structures of proteins. Macromolecules 1976;9:945–950.
33. Miyazawa S, Jernigan RL. Estimation of effective inter-residue contact energies from protein crystal structures: quasi-chemical approximation. Macromolecules 1985;18:534–552.
34. Sippl MJ. Knowledge-based potentials for proteins. Curr Opin Struct Biol 1995;5:229–235.
35. Thomas PD, Dill KA. Statistical potentials extracted from protein structures: how accurate are they? J Mol Biol 1996;257:457–469.
36. Betancourt MR, Thirumalai D. Pair potentials for protein folding: choice of reference states and sensitivity of predicted native states to variations in the interaction schemes. Protein Sci 1999;8:361–369.
37. Kolinski A, Godzik A, Skolnick J. A general method for the prediction of the three dimensional structure and folding pathway of globular proteins: application to designed helical proteins. J Chem Phys 1993;98:7420–7433.
38. Gan HH, Tropsha A, Schlick T. Lattice protein folding with two and four-body statistical potentials. Proteins 2001;43:161–174.
39. Vendruscolo M, Najmanovich R, Domany E. Can a pairwise contact potential stabilize native protein folds against decoys obtained by threading? Proteins 2000;38:134–148.
40. Wood RH, Thompson PT. Differences between pair and bulk hydrophobic interactions. Proc Natl Acad Sci USA 1990;87:8921–8927.
41. Rapaport DC, Scheraga HA. Hydration of inert solutes: a molecular dynamics study. J Phys Chem 1982;86:873–878.
42. Wallqvist A. Molecular dynamics study of a hydrophobic aggregate in an aqueous solution of methane. J Phys Chem 1991;95: 8921–8927.
43. Wallqvist A. Molecular dynamics study of hydrophobic aggregation in water/methane/methanol systems. Chem Phys Lett 1991; 182:237–241.
44. Tsai J, Gerstein M, Levitt M. Simulating the minimum core for hydrophobic collapse in globular proteins. Protein Sci 1997;6: 2606–2616.
45. Raschke TM, Tsai J, Levitt M. Quantification of the hydrophobic interaction by simulations of the aggregation of small hydrophobic solutes in water. Proc Natl Acad Sci USA 2001;98:5965–5969.
46. Czaplewski C, Rodziewicz-Motowidlo S, Liwo A, Ripoll DR, Wawak RJ, Scheraga HA. Molecular simulation study of cooperativity in hydrophobic association. Protein Sci 2000;9:1235–1245.
47. Rank JA, Baker D. A desolvation barrier to hydrophobic cluster formation may contribute to the rate-limiting step in protein folding. Protein Sci 1997;6:347–354.
48. Forsman J, Jönsson B. Monte Carlo simulations of hydrophobic interactions: a test particle approach. J Chem Phys 1994;101: 5116–5125.
49. Shimizu S, Chan HS. Temperature dependence of hydrophobic interactions: a mean force perspective, effects of water density, and nonadditivity of thermodynamic signatures. J Chem Phys 2000;113:4683–4700.
50. Shimizu S, Chan HS. Configuration-dependent heat capacity of pairwise hydrophobic interactions. J Am Chem Soc 2001;123: 2083–2084.
51. Dill KA, Chan HS. From Levinthal to pathways to funnels. Nat Struct Biol 1997;4:10–19.
52. Onuchic JN, Luthey-Schulten Z, Wolynes PG. Theory of protein

folding: the energy landscape perspective. Annu Rev Phys Chem 1997;48:545–600.
53. Duan Y, Kollman PA. Pathways to a protein folding intermediate observed in a 1-microsecond simulation in aqueous solution. Science 1998;282:740–744.
54. Daggett V. Long timescale simulations. Curr Opin Struct Biol 2000;10:160–164.
55. Lee B, Richards FM. The interpretation of protein structures: estimation of static accessibility. J Mol Biol 1971;55:379–400.
56. Richards FM. Areas, volumes, packing and protein structure. Annu Rev Biophys Bioeng 1977;6:151–176.
57. Connolly ML. Solvent-accessible surfaces of proteins and nucleic acids. Science 1983;221:709–713.
58. Eisenberg D, McLahlan AD. Solvation energy in protein folding and binding. Nature 1986;319:199–203.
59. Ooi T, Oobatake M, Nemethy G, Scheraga HA. Accessible surface areas as a measure of the thermodynamic parameters of hydration of peptides. Proc Natl Acad Sci USA 1987;84:3086–3090.
60. Eisenhaber F, Argos P. Improved strategy in analytic surface calculation for molecular systems—handling of singularities and computational efficiency. J Comp Chem 1993;14:1272–1280.
61. Jackson RM, Sternberg MJE. Protein surface area defined. Nature 1993;366:638–638.
62. Jackson RM, Sternberg MJE. Application of scaled particle theory to model the hydrophobic effect—implications for molecular association and protein stability. Protein Eng 1994;7:371–383.
63. Gomez J, Hilser VJ, Xie D, Freire E. The heat capacity of proteins. Proteins 1995;22:404–412.
64. Hilser VJ, Gomez J, Freire E. Enthalpy change in protein folding and binding: refinement of parameters for structure-based calculations. Proteins 1996;26:123–133.
65. Hermann RB. Modeling hydrophobic solvation of nonspherical systems: comparison of use of molecular surface area with accessible surface area. *J Comp Chem* 1996;18:115–125.
66. Fukunishi Y, Suzuki M. Potential of mean force calculation of solute molecules in water by a modified solvent-accessible surface method. J Comp Chem 1997;18:1656–1663.
67. Hummer G. Hydrophobic force field as a molecular alternative to surface-area models. J Am Chem Soc 1999;121:6299–6305.
68. Lazaridis T, Karplus M. Effective energy functions for proteins in solution. Proteins 1999;35:133–152.
69. Lazaridis T, Karplus M. Heat capacity and compactness of denatured proteins. Biophys Chem 1999;78:207–217.
70. Lazaridis T, Karplus M. Discrimination of the native from misfolded protein models with an energy function including implicit solvation. J Mol Biol 1999;288:477–487.
71. Roux B, Simonson T. Implicit solvent models. Biophys Chem 1999;78:1–20, and references therein.
72. Shimizu S, Ikeguchi M, Nakamura S, Shimizu K. Size dependence of transfer free energies: a hard-sphere-chain-based formalism. J Chem Phys 1999;110:2971–2982.
73. Daura X, Mark AE, van Gunsteren WF. Peptide folding simulations: no solvent required? Comput Phys Commun 1999;123:97–102.
74. Lee CY, McCammon JA, Rossky PJ. The structure of liquid water at an extended hydrophobic surface. J Chem Phys 1984;80:4448–4455.
75. Cheng Y-K, Rossky PJ. Surface topography dependence of biomolecular hydrophobic hydration. Nature 1998;392:696–699.
76. Lum K, Chandler D, Weeks JD. Hydrophobicity at small and large length scales. J Phys Chem B 1999;103:4570–4577.
77. Southall NT, Dill KA. The mechanism of hydrophobic solvation depends on solute radius. J Phys Chem B 2000;104:1326–1331.
78. Jorgensen WL. BOSS, Version 4.1. New Haven, CT. Yale University; 1999.
79. Chan HS, Dill KA. Energy landscape and the collapse dynamics of homopolymers. J Chem Phys 1993;99:2116–2127.
80. Chan HS, Dill KA. Transition states and folding dynamics of proteins and heteropolymers. J Chem Phys 1994;100:9238–9257.
81. Chan HS, Dill KA. Solvation: how to obtain microscopic energies from partitioning and solvation experiments. Annu Rev Biophys Biomol Struct 1997;26:425–459, and references therein.
82. Lazaridis T, Karplus M. New view of protein folding reconciled with the old through multiple unfolding simulations. Science 1997;278:1928–1931.
83. Inuzuka Y, Lazaridis T. On the unfolding of α-lytic protease and the role of the PRO region. Proteins 2000;41:21–32.
84. Kuhlman B, Baker D. Native protein sequences are close to optimal for their structures. Proc Natl Acad Sci USA 2000;97:10383–10388. [Correction: 2000;97:13460.]
85. Hummer G, Garde S, Garcia AE, Pohorille A, Pratt LR. An information theory model of hydrophobic interactions. Proc Natl Acad Sci USA 1996;93:8951–8955.
86. Chan HS, Kaya H, Shimizu S. Computational methods for protein folding: scaling a hierarchy of complexities. In: Jiang T, Xu Y, Zhang MQ, editors. Current Topics in Computational Molecular Biology. Cambridge, MA: The MIT Press; 2002. p 403–447.
87. Young WS, Brooks CL. A reexamination of the hydrophobic effect: exploring the role of the solvent model in computing the methane-methane potential of mean force. J Chem Phys 1997;106:9265–9269.
88. Mahoney MW, Jorgensen WL. A five-site model for liquid water and the reproduction of the density anomaly by rigid, nonpolarizable potential functions. J Chem Phys 2000;112:8910–8922.
89. Sosnick TR, Trewhella J. Denatured states of ribonuclease A have compact dimensions and residual secondary structure. Biochemistry 1992;31:8329–8335.
90. Shortle D. Denatured states of proteins and their roles in folding and stability. Curr Opin Struct Biol 1993;3:66–74.
91. Hagihara Y, Hoshino M, Hamada D, Kataoka M, Goto Y. Chain-like conformation of heat-denatured ribonuclease A and cytochrome c as evidenced by solution X-ray scattering. Fold Des 1998;3:195–201.
92. Mok YK, Kay CM, Kay LE, Forman-Kay J. NOE data demonstrating a compact unfolded state for an SH3 domain under nondenaturing conditions. J Mol Biol 1999;289:619–638.
93. Choy WY, Forman-Kay JD. Calculation of ensembles of structures representing the unfolded state of an SH3 domain. J Mol Biol 2001;308:1011–1032.
94. Shimizu S, Chan HS. Reply to "Comment on 'Anti-cooperativity in hydrophobic interactions: a simulation study of spatial dependence of three-body effects and beyond." [J Chem Phys 116, 2665 (2002)] J Chem Phys 2002;116:2668–2669.
95. Czaplewski C, Rodziewicz-Motowidlo S, Liwo A, Ripoll DR, Wawak RJ, Scheraga HA. Comment on "Anti-cooperativity in hydrophobic interactions: a simulation study of spatial dependence of three-body effects and beyond" [J Chem Phys 115, 1414 (2001)]. J Chem Phys 2002;116:2665–2667.
96. Jorgensen WL, Chandrasekhar J, Madura JD, Impey RW, Klein ML. Comparison of simple potential functions for simulating liquid water. J Chem Phys 1983;79:926–935.
97. van Belle D, Wodak SJ. Molecular dynamics study of methane hydration and methane association in a polarizable water phase. J Am Chem Soc 1993;115:647–652.
98. Jungwirth P, Zahradnik R. The entropy driven hydrophobic effect as a function of solute-solvent interactions: a molecular dynamics study. Chem Phys Lett 1994;217:319–324.
99. Payne VA, Matubayasi N, Murphy LR, Levy, RM. Monte Carlo study of the effect of pressure on hydrophobic association. J Phys Chem B 1997;101:2054–2060.
100. Matubayasi N, Nakahara, M. Association and dissociation of nonpolar solutes in super- and subcritical water. J Phys Chem 2000;104:10352–10358.
101. Ghosh T, Garcia AE, Garde S. Enthalpy and entropy contributions to the pressure dependence of hydrophobic interactions. J Chem Phys 2002;116:2480–2486.
102. Zichi DA, Rossky PJ. The equilibrium solvation structure for the solvent-separated hydrogen bond. J Chem Phys 1985;83:797–808.
103. Head-Gordon T. Is water structure around hydrophobic group clathrate like? Proc Natl Acad Sci USA 1995;92:8308–8312.
104. Leikin S, Parsegian VA, Rau DC, Rand RP. Hydration forces. Annu Rev Phys Chem 1993;44:369–395.
105. Czaplewski C, Ripoll DR, Liwo A, Rodziewicz-Motowidlo S, Wawak J, Scheraga HA. Can cooperativity in hydrophobic association be reproduced correctly by implicit solvation models? Int J Quantum Chem 2002;88:41–45.